Author(s): Napari, Mari; Tarvainen, Olli; Kinnunen, Sami; Arstila, Kai; Julin, Jaakko; Fjellvåg, Ø. S.; Weibye, K.; Nilsen, O.; Sajavaara, Timo

Title: The α and γ plasma modes in plasma-enhanced atomic layer deposition with O2–N2 capacitive discharges

Year: 2017

Version:

Please cite the original version:

Napari, M., Tarvainen, O., Kinnunen, S., Arstila, K., Julin, J., Fjellvåg, Ø. S., Weibye, K., Nilsen, O., & Sajavaara, T. (2017). The α and γ plasma modes in plasma-enhanced atomic layer deposition with O2–N2 capacitive discharges. Journal of Physics D: Applied Physics, 50(9), Article 095201. https://doi.org/10.1088/1361-6463/aa59b3

The α and γ plasma modes in plasma-enhanced atomic layer deposition with O_2–N_2 capacitive discharges

M Napari[1], O Tarvainen[1], S Kinnunen[1], K Arstila[1], J Julin[1]‡, Ø S Fjellvåg[2], K Weibye[2], O Nilsen[2], and T Sajavaara[1]

[1] Department of Physics, University of Jyväskylä, P. O. Box 35, 40014 University of Jyväskylä, Finland

[2] Department of Chemistry, University of Oslo, P. O. Box 1033, 0315 Oslo, Norway

E-mail: mari.napari@jyu.fi

Abstract. Two distinguishable plasma modes in the O_2–N_2 radio frequency capacitively coupled plasma (CCP) used in remote plasma-enhanced atomic layer deposition (PEALD) were observed. Optical emission spectroscopy and spectra interpretation with rate coefficient analysis of the relevant processes were used to connect the detected modes to the α and γ modes of the CCP discharge. To investigate the effect of the plasma modes on the PEALD film growth, ZnO and TiO_2 films were deposited using both modes and compared to the films deposited using direct plasma. The growth rate, thickness uniformity, elemental composition, and crystallinity of the films were found to correlate with the deposition mode. In remote CCP operations the transition to the γ mode can result in a parasitic discharge leading to uncontrollable film growth and thus limit the operation parameters of the capacitive discharge in the PEALD applications.

Plasma-enhanced atomic layer deposition, capacitive discharges, plasma mode transition, zinc oxide, titanium dioxide

Submitted to: *J. Phys. D: Appl. Phys.*

‡ Present address: Institute of Ion Beam Physics and Materials Research, Helmholtz-Zentrum Dresden-Rossendorf, P. O. Box 510119, 01314 Dresden, Germany

1. Introduction

Plasma-enhanced atomic layer deposition (PEALD) is a chemical vapor deposition (CVD) technique that utilizes reactive plasma species for the growth of thin films. In PEALD subsequent pulses of the precursor and reactive plasma are separated with inert gas purges, ensuring surface limited growth and conformality [1]. PEALD is typically used when the deposition temperatures are limited lower than achievable with the thermal ALD, or in order to tune the film material properties.

The PEALD plasma processes can be divided into three categories: radical-enhanced, remote plasma, and direct plasma ALD, characterized by the contact between the plasma and the deposition surface and the type of plasma species accounting for the surface reactions during the film growth [2]. There are several equipment configurations for the plasma generation, of which the capacitively coupled plasma (CCP) is typically used in the direct plasma ALD whereby the deposition surface is positioned directly in the discharge volume between the parallel electrodes. The advantages of the CCPs include the low-cost, scalability, and repeatability [3]. To prevent direct contact between the plasma and deposition surface and thus to reduce the flux of energetic ions possibly causing damage to the substrate, a remote CCP approach (also referred as "triode" configuration, adapted from the PECVD processing [4, 5]) has been commercialized for PEALD [6]. In this configuration a perforated plate or a grid is placed between the powered electrode and the substrate. The grid acts as a grounded electrode, confining the plasma above it, still allowing the flux of the reactive neutral species, referred to as plasma radicals, to the substrate [7]. The grid however can change the properties of the capacitive discharge and may lead to discrepancies regarding the PEALD film growth. It has been suggested that this is caused by the formation of an active plasma between the grid and the substrate [8]. Here we show that the likely explanation for this "parasitic" discharge is the CCP mode transition.

It has been acknowledged that a radio frequency (RF) capacitive discharge can exist in several different modes. The electron heating mode can be either collisionless or collisional [9, 10, 11], and the power can be dissipated dominantly by the electrons in the bulk plasma or the ions in the plasma sheath [12]. In the low-current α mode the electrons sustaining the ionization acquire energy in the RF electric field within the plasma as well as in the oscillations of the near-electrode sheath boundary [13, 14, 15]. In the high-current γ mode the ionization occurs predominantly in the near-electrode sheaths, and is sustained by the electron avalanches developed by the secondary electrons emitted from the electrodes [14, 16]. These secondary electrons are created by the primary electron, ion, photon, and metastable neutral bombardment of the electrodes, preceded by a reduction of the sheath thickness or even sheath breakdown [17, 18]. The discharge transition from α to γ mode has been reported at pressures from 10^{-2} mbar up to atmospheric pressure, and its dependence on the operational parameters such as the gas composition, driving frequency, and power input has been widely studied [16, 19, 20, 21, 22]. Besides the α and γ modes, also a so called δ mode has been

detected to exist in low-pressure plasmas of molecular gases. The δ mode can serve as an intermediate transition mode between the α and γ modes in the gases where the reaction products from electron impact dissociation possess lower ionization potential than the initial molecules [23, 24, 25].

In this work the modes in capacitively coupled O_2–N_2 plasma were studied with respect to the plasma-enhanced atomic layer deposition. Two different plasma modes were detected under typical PEALD operating conditions. The effect of the modes on the PEALD ZnO and TiO_2 film growth was investigated by means of commercial CCP PEALD reactor that can be operated using both the remote and direct plasma configurations. ZnO and TiO_2 films were chosen for the case study, as their PEALD processes and characteristics are well established [26, 27, 28, 29, 30, 31, 32]. The growth rate, composition, and structure of the films were characterized and found to correlate with the deposition plasma mode. This correlation and its connection to the α and γ modes of the capacitive RF discharge will be discussed in detail.

2. Methods

The plasma mode investigations and thin film depositions were performed using a commercial ALD reactor (Beneq TFS-200). The capacitively coupled plasma was generated between the powered ⌀=200 mm plate electrode and a grounded grid using CESAR 133 series 13.56 MHz radio frequency generator (Advanced Energy). The impedance matching to the plasma was realized with Navio Matching Network (Advanced Energy). Typical PEALD conditions were used for the experiments: O_2 ($\geq$ 99.999 % AGA HiQ) plasma gas flow was set to 50 sccm and the chamber pressure was maintained at ca. 4.5 mbar with a continuous 300 sccm flow of N_2 in addition to the process N_2 flow of 250 sccm ($N_2 \geq$ 99.999 % from nitrogen generator Inmatec IMT-PN 1150). The grid (aperture diameter 1.5 mm, spacing 2.0 mm, grid transparency ca. 50 %) was positioned 10 mm above the deposition surface, and the electrode–grid distance was fixed at 35 mm. The schematic of the PEALD reactor setup is shown in figure 1.

2.1. Plasma mode characterization

2.1.1. Experimental methods To investigate the plasma properties, VIS spectra (300–875 nm) of the plasma were measured with optical emission spectroscopy (OES). The OES measurements were performed with Ocean Optics USB2000+ spectrometer (custom configuration, grating 600 mm^{-1}, 25 μm slit, range 200–875 nm with nominal resolution of 1.4 nm.) The optical fiber (300–1100 nm) was positioned to view the plasma perpendicularly through the powered electrode at 40 mm radial distance from the electrode center. The optical fiber was coupled to the plasma gas feedthrough pipe (inner diameter 4 mm) with a quartz vacuum window and a Thorlabs F220SMA-A coupler, and the distance from the plasma volume to the coupler was 35 cm. The OES

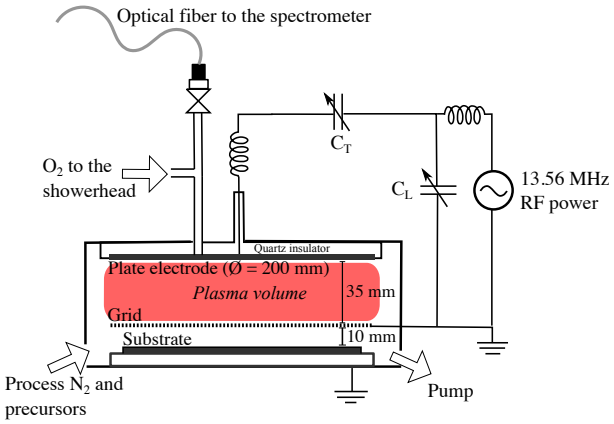

Figure 1. A schematic illustration of the remote capacitively coupled PEALD setup used in the study.

setup was designed to ensure that only the photons yielding from the plasma reactions close to the electrode center were measured. Besides the OES measurement the self-bias voltage of the powered electrode was measured during the discharge using the integrated control system of the PEALD reactor.

2.1.2. Rate coefficient analysis Rate coefficient analysis was carried out to interpret the measured OES spectra. The total volumetric rate of an electron-molecule collision process in the plasma, assuming stationary molecules, $v_e >> v_n$, can be expressed as

$$R = n_e n_n \int f_e(v)\ v\ \sigma(v)\ \mathrm{d}v = n_e n_n \langle \sigma v \rangle\ , \tag{1}$$

where n_e and n_n are the densities of the electrons and neutral species, respectively, $v = v_e$ is the electron velocity, $\sigma(v)$ is the process cross section, and f_e the electron energy/velocity distribution function (EEDF/EVDF). In this work all the rate coefficients $\langle \sigma v \rangle$ were calculated assuming a Maxwell-Boltzmann EVDF:

$$f_e(v) = 4\pi \left(\frac{m_e}{2\pi k T_e}\right)^{\frac{3}{2}} v^2 \exp\left(-\frac{m_e v^2}{2kT_e}\right)\ , \tag{2}$$

where kT_e is the electron temperature. From (1) and (2) it follows for the rate coefficient $\langle \sigma v \rangle$

$$\langle \sigma v \rangle = 4\pi \left(\frac{m_e}{2\pi k T_e}\right)^{\frac{3}{2}} \int v^3 \sigma(v) \exp\left(-\frac{m_e v^2}{2kT_e}\right) \mathrm{d}v\ . \tag{3}$$

The rate coefficients from (3) were solved numerically for the electron-molecule collision processes corresponding to the detected optical emission lines in the plasma using the cross sections $\sigma(v)$ reported in the literature.

2.2. PEALD thin films

2.2.1. Film deposition All the films were deposited on Si (100) substrates with a native surface oxide using the PEALD reactor setup described above. The O_2 plasma gas and

the N_2 process gas flows, and the electrode–grid geometry were the same as in the OES measurements. The plasma ignition was controlled by manually tuning the variable capacitors of the L-type matching network so that the plasma ignited repeatedly in the mode under investigation throughout the deposition cycles. The so called 'tune' capacitor C_T was kept at constant value, while the 'load' capacitor C_L value was varied. The plasma mode was also continuously monitored with the OES. Besides the mode-specific depositions, also films with direct plasma were grown under the same operation settings. For these depositions the grid was removed and the electrode was lowered to a distance of 35 mm from the deposition surface to maintain an equivalent discharge geometry. ZnO films were deposited at 50 °C using diethylzinc (DEZ, $(C_2H_5)_2Zn$) metal precursor ($\geq$ 95 % Strem Chemicals Inc.) and O_2 plasma. TiO_2 films were deposited at 150 °C with $TiCl_4$ metal precursor (99.9 % Sigma-Aldrich) and O_2 plasma. For each film 1000 PEALD cycles were deposited with the delivered plasma power of 150 W, which was chosen to ensure the stability of both plasma modes without varying the power input. Each PEALD cycle consisted of 0.4 s precursor pulse followed by 5 s N_2 purge, the O_2 flow (50 sccm) was turned on 3 s prior to the plasma ignition and the plasma pulse length was 3 s, followed again by 5 s N_2 purge. During the precursor pulsing a N_2 flow of 10 sccm was fed to the plasma gas feedtrough to prevent the film deposition on the OES vacuum window.

2.2.2. Film characterization Film thicknesses were measured using optical ellipsometer (Rudolph AutoEL III, laser wavelength 632.8 nm). Time-of-flight elastic recoil detection analysis (ToF-ERDA) was used to discover the elemental compositions of the films [33]. The ion beams for measuring the composition of the ZnO and TiO_2 films were 13.6 MeV $^{79}Br^{7+}$ and 10.2 MeV $^{63}Cu^{5+}$, respectively, and the data was analyzed using Potku analysis software [34]. Powder X-ray diffraction (XRD) and grazing incidence angle X-ray diffraction (GIXRD) measurements were done using Bruker AXS D8 Discover (XRD) and PanAnalytical Empyrean (GIXRD), both with Cu Kα_1 (8.047 keV) as incident X-ray. X-ray photoelectron spectroscopy (XPS) measurements were performed with Theta Probe by ThermoScientific with Al Kα_1 (1.487 keV) as incident X-ray, and 4 keV Ar^+ beam was used for surface cleaning by sputtering. The film surface morphology was studied with helium ion microscopy (HIM, Zeiss Orion NanoFab) using 30 keV He^+ beam with beam current of ca. 0.25 pA.

3. Results

3.1. Plasma mode analysis

In the OES measurements two different modes of the O_2–N_2 plasma were detected. In these modes the plasma differs in color as well as in the total optical emission intensity. Figure 2 shows examples of the measured spectra of the low- and high- intensity mode plasmas. The low-intensity mode was primarily observed with low RF power of 50–

150 W, while the plasma ignition into the high-intensity mode started to dominate when the power was increased above 200 W. Tuning of the matching circuit capacitors enabled choosing either the low- or high- intensity mode at delivered (forward - reflected) powers between 150 and 300 W. However, at high delivered powers (>250 W) the low-intensity mode was susceptible to undergo a transition to high-intensity mode within the plasma pulse regardless of the capacitor tuning. It was also observed that the increase in the optical emission intensity was accompanied by a significant increase in the measured self-bias voltage shown in figure 3. The difference in the self-bias voltages between the two modes was also observed to increase when the pressure was decreased.

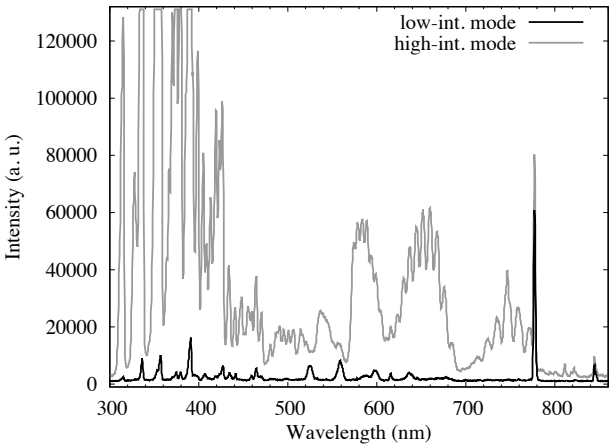

Figure 2. The spectrometer integration time normalized optical emission spectra of the low- and high-intensity modes of the O_2–N_2 plasma measured with 220 W delivered power at pressure of 4.5 mbar. The most intense lines of high-intensity mode spectrum are saturated.

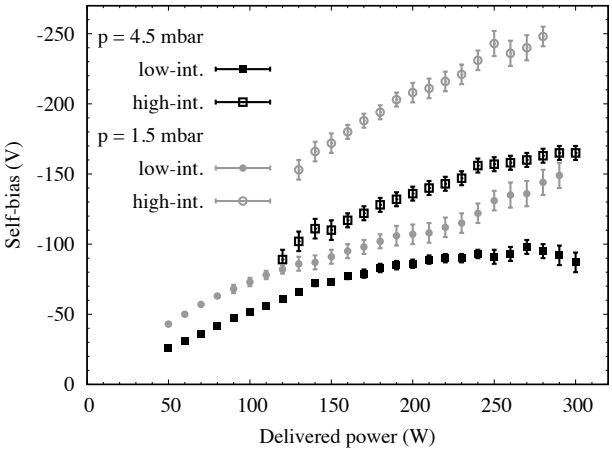

Figure 3. The self-bias voltage of the powered electrode as a function of the delivered power in the low- and high-intensity mode plasmas at pressures of 1.5 and 4.5 mbar. Error bars correspond to the pulse-to-pulse variation.

The normalized optical emission spectra of the low- and high-intensity plasma modes measured with 150 W delivered power are presented in figure 4 with the most

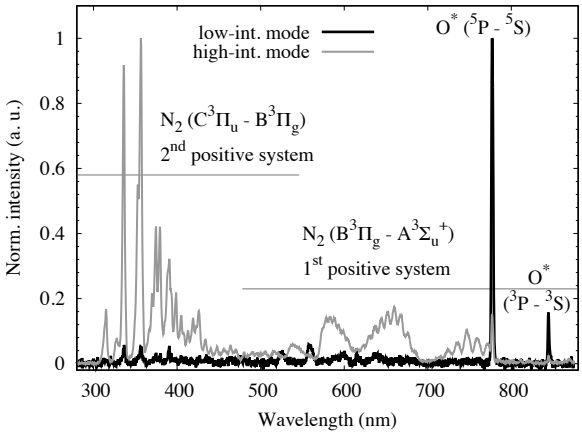

Figure 4. The optical emission spectra of the O_2–N_2 plasma in low- and high-intensity modes, normalized to the highest intensity line of each spectrum. The electronic transmissions corresponding to the most intense atomic lines and molecular bands are labeled.

intense atomic emission lines and molecular emission bands identified. The spectrum in the low-intensity mode is dominated by the $2p^3\ ^5P \rightarrow 2p^3\ ^5S$ and $2p^3\ ^3P \rightarrow 2p^3\ ^3S$ transitions of atomic oxygen at 777 nm and 845 nm, respectively, whereas in the high-intensity mode the spectrum is dominated by the emission by electronically excited N_2 molecules.

3.1.1. Low-intensity mode Although the molecular and atomic optical emissions of O_2 and O occur predominantly in the UV/VUV range, the dominance of the atomic emission in the VIS-spectrum of the low-intensity mode indicates significant dissociation degree of the oxygen gas. The two major electron-collision processes in low-temperature plasma accounting for the dissociation of the ground state $O_2(X^3\Sigma_g^-, \nu)$ are the dissociative electron attachment (DEA) $e^- + O_2 \rightarrow O_2^{-*} \rightarrow O^-(^2P) + O(^3P)$ and the electron impact dissociation (EID) $e^- + O_2 \rightarrow O_2^{-*} \rightarrow 2O(^3P) + e^-$, where the (^3P) and (^2P) refer to the ground states of the neutral O and O^- ion, respectively. The DEA and EID processes can also occur from the metastable $O_2(a^1\Delta_g)$ state, which is created by the electronic excitation $e^- + O_2(X^3\Sigma_g^-) \rightarrow O_2(a^1\Delta_g) + e^-$. The relevance of the different electron impact processes can be resolved by comparing their rate coefficients $\langle \sigma v \rangle$. The vibrationally resolved rate coefficients of the DEA and EID from the ground state (reported recently by Laporta et al. [35, 36]) and metastable states as well as the excitation to the metastable state [37] are visualized in figure 5.

The rate coefficient of the ground state DEA exceeds the rate coefficient of EID at each vibrational level ν, differing by two orders of magnitude at low electron temperatures and high vibrational levels. The processes involving metastable O_2 can also be considered significant. However, it can be assumed that the density of the metastable $O_2(a^1\Delta_g)$ in the plasma is always less than the density of the ground state O_2. This

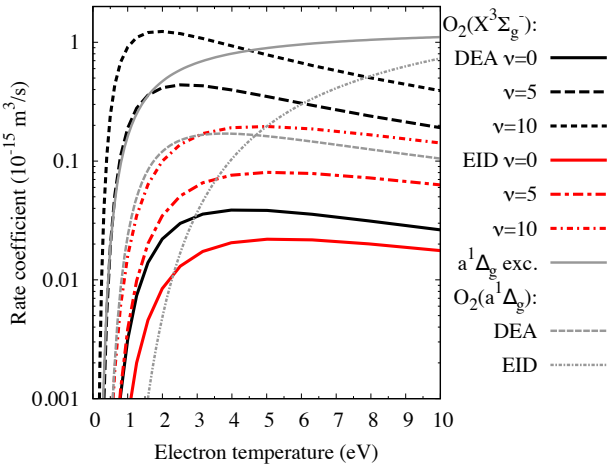

Figure 5. Rate coefficients of O_2 dissociative electron attachment (DEA) and electron impact dissociation (EID) processes of the ground state $O_2(X^3\Sigma_g^-, \nu)$ at vibrational levels ν=0, 5, and 10, the electronic excitation to the metastable state $O_2(a^1\Delta_g)$, and the DEA and EID from the $O_2(a^1\Delta_g)$ state.

is due to the continuous flow of O_2 into the plasma volume as well as quenching of the metastable molecules by collisions in the plasma and in interactions with the surfaces. As the vibrational level of the ground state molecule has a significant impact on the rate coefficient of the subsequent collisional processes, different mechanisms resulting in vibrational excitation should be taken into account. The vibrational heating of the ground state O_2 occurs via two channels: the excitation to electronic states followed by radiative decay to a higher vibrational level, and the resonant excitation by low-energy electron scattering. The electronic excitation reactions have a threshold energy of ∼10 eV, whereas the cross sections of the resonant processes peak at energies on the order of 1 eV, depending on the initial and final vibrational levels ν and ν', respectively [38]. As seen in figure 6, the rate coefficients of the vibrational heating by $\Delta\nu$=1 are several orders of magnitude higher than the rate coefficients of the DEA process up to ν=10. Hence, it can be expected that these higher vibrational levels are heavily populated, subsequently increasing the total volumetric rate of the following dissociation processes.

The high intensities of the O* decays ($2p^3\ ^5P \rightarrow 2p^3\ ^5S$ for 777 nm and $2p^3\ ^3P \rightarrow 2p^3\ ^3S$ for 845 nm emission) from excited states with 10.74 eV and 10.99 eV of energy, respectively, can not be explained solely by direct electron impact excitation of ground state O nor cascading from the upper states [39, 40]. The main process producing the detected excited O* radicals is considered to be mutual neutralization of the positive and negative oxygen ions ($O^+ + O^- \rightarrow O^* + O$) [41]. This process corresponds to a release of 11.6 eV chemical potential, enough to occupy the emitting $2p^3\ ^5P$ and $2p^3\ ^3P$ states with theoretical rate coefficients of 3.3–8.3·10^{-13} m^3/s and 0.8–2.2·10^{-13} m^3/s at ∼0.1–1 eV ion temperature, respectively [41, 42]. The dominance of these emission lines implies the DEA process via the presence of the O^- ions in the plasma. This

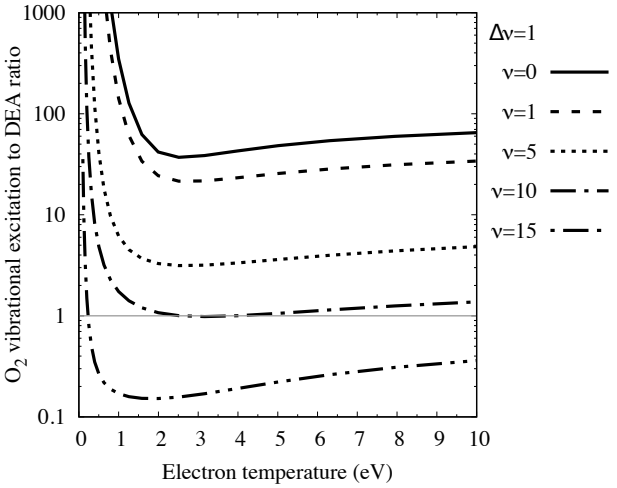

Figure 6. Ratio of rate coefficients for O_2 vibrational excitation $[e^- + O_2(X^3\Sigma_g^-, \nu) \rightarrow e^- + O_2(X^3\Sigma_g^-, \nu')]$ by $\nu \rightarrow \nu' = \Delta\nu = 1$ and DEA process from the corresponding initial vibrational level ν.

is also supported by the self-bias voltage results presented in figure 3. The negative self-bias builds up to compensate different mobilities of the electrons and ions collected by the powered electrode over each half-cycle of RF period. In electron-ion plasmas a higher self bias is required to compensate the fluxes in comparison to electronegative plasmas where a significant fraction of negative charge is carried by ions, which have lower mobility than electrons. The dissociative electron attachment, which was shown to be the main process for the production of the O^* emission measured in the low-intensity mode, results also in the formation of electronegative plasma. It has also been shown by simulations that the O^- density is comparable to the electron density in the O_2–N_2 mixture discharges even at low oxygen concentrations [43].

3.1.2. High-intensity mode The high-intensity mode was observed both as an increase in the total optical intensity and as a change in the optical emission spectrum that is dominated by the decays of excited states of N_2, the 1st ($B^3\Pi_g \rightarrow A^3\Sigma_u^+$) and the 2nd positive systems ($C^3\Pi_u \rightarrow B^3\Pi_g$) at 478–2531 nm (infra-red range not measured) and 268–546 nm, respectively (figure 4). To estimate the changes in the plasma properties the O_2 DEA rate coefficients were compared to the rate coefficients of the $e^- + X^1\Sigma_g^+ \rightarrow B^3\Pi_g + e^-$ and $e^- + X^1\Sigma_g^+ \rightarrow C^3\Pi_u + e^-$ electronic excitations of N_2 [36] and the total electron impact ionization of O_2 and N_2 calculated from the experimental cross section data from [44, 45]. As shown in figure 7, the O_2 DEA dominates over the excitations of N_2 at low electron temperatures and high vibrational levels of O_2. When the electron temperature exceeds 6 eV ionization becomes the dominant electron impact process. At electron temperatures above 3 eV, where the electronic excitations of N_2 dominate over the dissociation of O_2, the situation corresponds to the measured optical emission spectrum in the high-intensity mode. The total volumetric rate of each process depends on the plasma electron density n_e and the neutral density n_n as shown

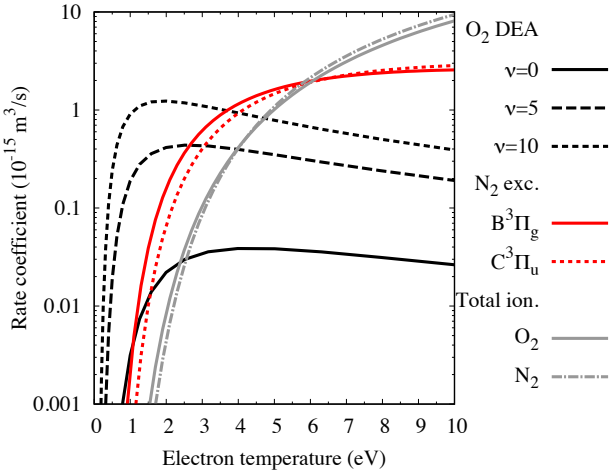

Figure 7. The rate coefficients for the total ionization of O_2 and N_2 and the excitation rate coefficients of $B^3\Pi_g$ and $C^3\Pi_u$ states illustrated against the rate coefficients of the O_2 DEA process at vibrational levels ν=0, 5, and 10.

in (1). In this case the neutral N_2 is always more abundant than O_2, i. e. $n_{n,N_2} > n_{n,O_2}$, due to the flow ratios of the plasma and process gases, which slightly decreases the threshold energy of the N_2 excitation dominance over the O_2 DEA in the terms of the actual process rate. The vibrational excitation can also result in small change in the rate coefficients of the N_2 electronic excitations, but the determination of this effect is complex due to the multiplicity of the possible ν , ν' combinations and their Frank-Condon factors [46]. These rate coefficients are, however, affected less by the initial vibrational level in comparison the dissociation processes of O_2 [47].

Altogether, the changes in the optical emission spectra imply that the average electron temperature within the plasma volume visible to the spectrometer increases when the plasma transition to the high-intensity mode occurs. The maximum effective electron temperature can be estimated to be below ∼9 eV, based on the dominance of the N_2 337.1 nm emission line from $C^3\Pi_u,\ \nu = 0 \rightarrow B^3\Pi_g,\ \nu' = 0$ transition over the line at 391.4 nm from the 1st negative system of N_2^+ ($B^2\Sigma_u^+,\ \nu = 0 \rightarrow X^2\Sigma_g^+,\ \nu' = 0$) in the spectrum (figure 4). The emission rate coefficients for the electron collision processes $e^- + N_2 \rightarrow N_2(C \rightarrow B + h\nu$@337.1 nm) and $e^- + N_2 \rightarrow N_2^+(B \rightarrow X + 2e^- + h\nu$@391.4 nm) are shown in figure 8. The rate coefficients are calculated from the experimental emission cross sections (Q_{emis}) presented in [45].

3.2. PEALD growth

To investigate whether the detected changes in the plasma operated in the low- and high-intensity modes affect the PEALD film growth with the remote CCP, two sets of oxide thin films, ZnO and TiO_2, were deposited. Low deposition temperatures, 50 °C and 150 °C for ZnO and TiO_2, respectively, were chosen to enhance the effect of the plasma over the thermally driven ALD reactions. Each set consisted of three 1000 cycle depositions, one with the detected low-intensity plasma mode (LI), one with high-

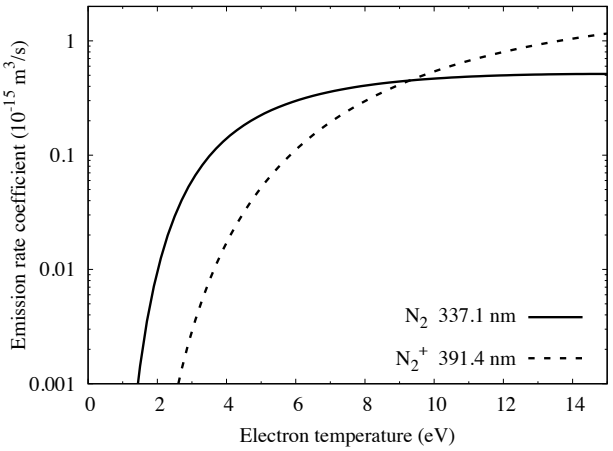

Figure 8. Emission rate coefficients for N_2 337.1 nm ($C^3\Pi_u,\ \nu = 0 \rightarrow B^3\Pi_g,\ \nu' = 0$) and N_2^+ ($B^2\Sigma_u^+, \nu = 0 \rightarrow X^2\Sigma_g^+, \nu' = 0$) 391.4 nm lines.

intensity plasma mode (HI), and one with direct plasma with the grid removed. It was observed that with the direct plasma the plasma was invariably ignited in the low-intensity mode, independent on the matching network tuning.

3.2.1. ZnO films Figure 9 shows the thicknesses of the ZnO films deposited on quarters of 150 mm Si wafers, measured as a function of the radial distance from the wafer and reactor/electrode center. The film deposited with the low-intensity plasma mode exhibits a uniform thickness throughout the substrate area, with an estimated growth per cycle (GPC) value of ca. 0.85 Å. A uniform film was also achieved by deposition with direct plasma, with GPC of 1.45 Å. In both cases the GPC value is less than previously reported (1.5–2.5 Å) for PEALD ZnO at 100 °C with DEZ + O_2 plasma [48, 26, 49] and (1.5–2.9 Å) at temperatures from 25 to 85 °C when dimethylzinc ($(CH_3)_2Zn$) was used as metal precursor [50]. Both the precursor and deposition temperature affect the ZnO film growth, but the higher deposition rate in the literature can also be caused by a different plasma reactor configuration in the studies where DEZ precursor was used. These studies utilized inductively coupled plasma (ICP) in which the plasma density is typically higher than in CCP [3]. In the film deposited with the high-intensity mode plasma pulses a significant radial non-uniformity was measured. In the region close to the electrode center the film corresponds seemingly to the film deposited with the direct plasma, whereas at the edges of the wafer the film thickness is similar to the remote low-intensity plasma mode deposited film.

The ToF-ERDA measured elemental compositions of the ZnO films, analyzed from the film bulk excluding the possible surface and interface impurities, are presented in table 1. Similarly to the thickness measurements, the correspondences between the low-intensity mode plasma deposited film and the edges of the high-intensity mode deposited film were detected, as well as between the samples from center of the film deposited with the high-intensity mode and the film grown using direct plasma. The O:Zn ratio of the

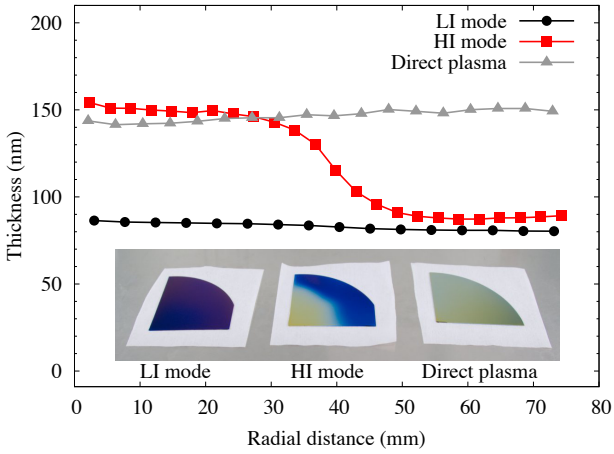

Figure 9. Thicknesses of 1000 PEALD cycle ZnO films deposited with remote low- and high-intensity mode plasma (LI and HI, respectively), and with a direct plasma, measured as a function of the distance from the reactor center. Inset: a photograph of the corresponding ZnO films on 1/4 of 150 mm Si wafers.

low-intensity mode PEALD film deviates from the 1:1 of the stoichiometric ZnO. The film has also a high concentration of light element impurities (hydrogen, carbon, and nitrogen). The XPS spectra of the films are shown in figure 10. The intensity of the C 1s peak at 290.5 eV from the carbonaceous species in the low-intensity mode film, as well as in the edges of the high-intensity mode film is significantly reduced in the direct plasma deposited sample and in the high-intensity mode film center. A similar reduction can also be seen in the high binding energy tail of the O 1s spectra attributed to OH^- and carbonate C-O and C=O bonds [51, 52]. The small nitrogen incorporation can be attributed either to the CN species [53] or to the substitution of nitrogen molecules into the oxygen sites in the ZnO [54]. High H and C concentrations in the low-temperature PEALD oxide films from metal-organic precursors have also been reported earlier [55, 56]. These are attributed to the residues of the precursor ligands remaining in the film after the plasma pulse and can be explained by the incomplete surface reactions between the metal precursor and the O_2 plasma [57]. In the film deposited with the direct plasma the composition is closer to stoichiometric with the reduced impurity content indicating that the oxidizing surface reactions are enhanced with the presence of the active plasma.

Table 1. The elemental composition of the ZnO films, deposited with low-intensity mode (LI), high-intensity mode (HI), and direct plasma.

Sample	H (at.-%)	C (at.-%)	N (at.-%)	O (at.-%)	Zn (at.-%)	O/Zn ratio
LI mode	13 ± 1	5.6 ± 0.5	1.4 ± 0.2	50 ± 2	30 ± 2	1.7 ± 0.2
HI mode (edge)	11 ± 1	4.3 ± 0.5	2.1 ± 0.2	49 ± 2	34 ± 2	1.5 ± 0.2
HI mode (center)	3 ± 0.5	0.5 ± 0.2	0.2 ± 0.1	52 ± 2	45 ± 2	1.2 ± 0.2
Direct plasma	4 ± 0.5	0.5 ± 0.2	0.4 ± 0.1	51 ± 2	44 ± 2	1.2 ± 0.2

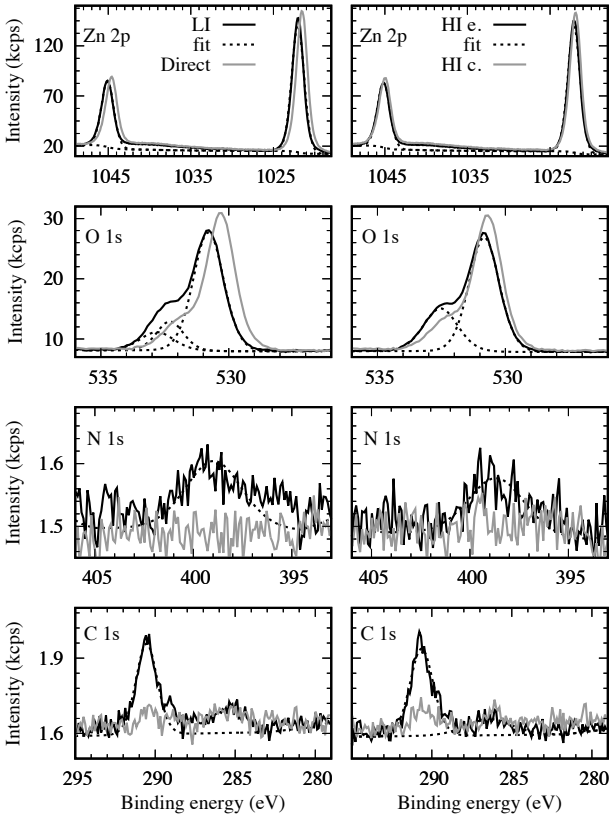

Figure 10. The Zn 2p, O 1s, N 1s, and C 1s XPS spectra of the ZnO films deposited with low-intensity mode (LI) and direct plasma (left) and high-intensity mode plasma (HI) with samples from the edge and the center of the wafer (right).

Similar correlation with the plasma conditions was found to extend to structural properties of the films, studied with XRD and HIM. Figures 11 (a) and (b) present the XRD patterns of the films. All the films were polycrystalline with hexagonal wurtzite structure. In the ZnO film deposited with the low-intensity mode, similarly to the edges of the high-intensity mode deposited film, the peak originating from the (002) reflection was observed, whereas the samples from the center of the high-intensity mode and direct plasma films exhibit strongly both the *a*- and *c*-axis orientation, shown as intense (100) and (002) peaks, respectively. When the morphology of the films are inspected (figures 12(a)–(d)) it can be seen that besides an increase in the surface roughness the film surface does not significantly change despite the distinction of the crystal structure. The elongated grains detected in the case of the thermal ALD ZnO [58, 59] were not observed in these films but the morphology with small grain size corresponded to what has been reported in the case of PEALD ZnO at higher temperatures [28]. The enhanced polycrystalline structure is, however, visible in the film cross-sections, shown in the insets of figure 12(a)–(d).

The crystal orientation of the ZnO films deposited with thermal ALD has been reported to depend on the deposition temperature [58, 60], the number of the ALD cycles (film thickness) [59, 61] and the substrate material [62]. It has also been discussed

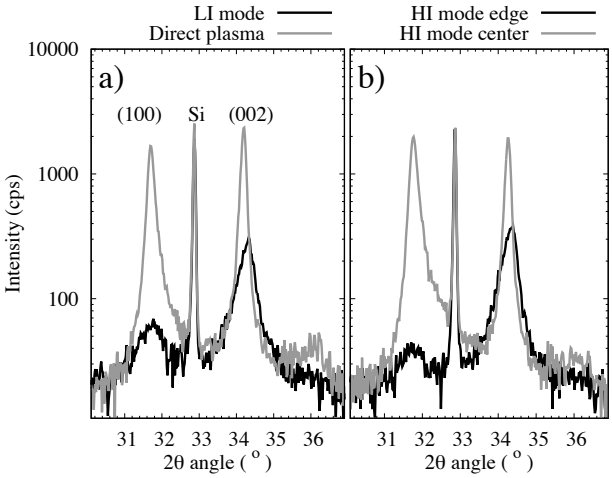

Figure 11. XRD patterns of the PEALD ZnO films deposited with (a) low-intensity mode plasma (LI) and direct plasma and (b) high-intensity mode plasma (HI).

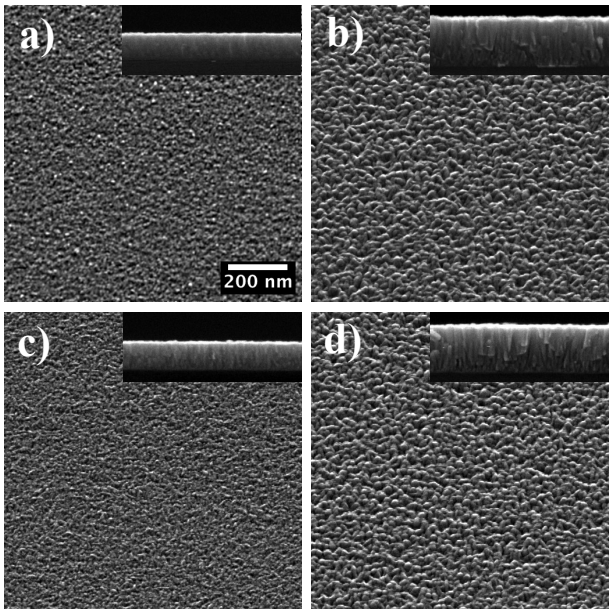

Figure 12. The surface structure HIM images of the ZnO films deposited with a) low-intensity mode, b) direct plasma, and c) and d) high-intensity mode plasma, samples from the (c) edge and (d) center of the wafer. The insets show the cross-sections of the corresponding films. The samples are tilted to 45° and 90° for the surface and cross-section imaging, respectively, and the scale bar is 200 nm.

that different densities of the *a*- and *c*-oriented ZnO crystals affect the overall ALD growth rate [58, 62]. For PEALD ZnO films deposited at temperatures from 100 °C to 300 °C the (002) has been reported to be the dominant orientation when remote ICP plasma has been used [26, 49], but also (100) orientation has been detected in the films deposited at lower temperatures [48]. Here, the crystal growth of the ZnO appears to be dependent on the plasma operation conditions, where the presence of direct plasma results in enhanced crystallinity without preferred orientation. However,

direct comparison between different studies is complicated as the plasma properties that affect the film growth, such as the ion flux to the deposition surface, are strongly reactor configuration dependent [62].

3.2.2. TiO_2 films Figure 13 presents the thicknesses of the TiO_2 films as a function of the radial distance from the electrode center. As in the case of the ZnO, the films deposited either with remote low-intensity mode or with the direct plasma are of uniform thickness, even though the deposition parameters were not optimized for the TiO_2 growth. The GPC were measured to be ca. 0.57 Å and 0.87 Å for the low-intensity mode plasma deposited TiO_2 film and for the direct plasma deposited film, respectively. The GPC values are comparable with the earlier reports of PEALD TiO_2 from $TiCl_4$ precursor at temperatures below 200 °C [31, 32]. The radial thickness distribution of the high-intensity mode TiO_2 film differs from what was measured for the ZnO deposited under the same plasma conditions. The possible reason is the disturbed surface adsorption of the $TiCl_4$ during the precursor pulsing due to the N_2 flow through the OES measurement viewport or to the non-uniform plasma conditions during the plasma pulses. However, as seen with the ZnO films, the significant thickness non-uniformity is detected solely in the film deposited with the high-intensity mode plasma.

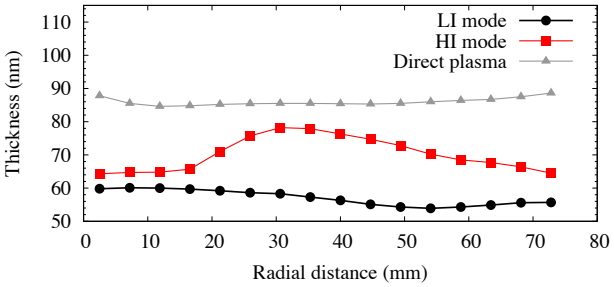

Figure 13. Thicknesses of the 1000 PEALD cycle TiO_2 films deposited with remote low- and high-intensity mode plasma (LI and HI, respectively), and direct plasma, measured as function of distance of from the reactor center.

In the case of the TiO_2 films the elemental composition, characterized using ToF-ERDA, was independent on the deposition plasma mode (table 2). All the films, including the films grown with direct plasma were close to the stoichiometric TiO_2, with total impurity (H, C, N, Cl) concentrations of less than 1.5 at.-%. The slightly increased N content in the direct plasma and in the thicker regions of the high-intensity mode deposited films is due to the formation of the Ti–N bonds, which were observed by the XPS measurements. The XPS N 1s and Ti 2p spectra indicated the incorporation of the TiN/TiON compounds. While all having alike elemental composition, the structural properties of the films appeared to correlate with the deposition plasma mode. GIXRD patterns of the TiO_2 films are presented in figures 14(a) and (b), and the surface morphology of the films deposited under different plasma conditions are compared in figures 15(a)–(d). The low-intensity mode film appears amorphous with a smooth

Table 2. The elemental composition of the TiO_2 films, deposited with low-intensity mode (LI), high-intensity mode (HI), and direct plasma.

Sample	H (at.-%)	C (at.-%)	N (at.-%)	Cl (at.-%)	O (at.-%)	Ti (at.-%)	O/Ti ratio
LI mode	0.1 ± 0.05	< 0.05	0.1 ± 0.05	0.3 ± 0.1	67 ± 2	32 ± 2	2.1 ± 0.2
HI mode (edge)	0.2 ± 0.1	0.1 ± 0.05	0.1 ± 0.05	0.3 ± 0.1	68 ± 2	32 ± 2	2.1 ± 0.2
HI mode (center[a])	0.4 ± 0.1	0.1 ± 0.05	1.0 ± 0.1	0.1 ± 0.05	67 ± 2	31 ± 2	2.2 ± 0.2
Direct plasma	0.1 ± 0.05	0.1 ± 0.05	1.0 ± 0.1	0.1 ± 0.05	68 ± 2	31 ± 2	2.2 ± 0.2

[a] Sample measured from the thickest film region.

surface, as seen both in the XRD pattern (figure 14(a)) and HIM micrograph (figure 15(a)). The GIXRD pattern of the direct plasma TiO_2 film in figure 14(a) shows the diffraction peaks (101), (004), (200), (105), and (211) of the anatase phase TiO_2. The crystallinity of the film is also visible in the HIM micrograph of the film surface (figure 15(b)). Instead, in the high-intensity mode the situation is somewhat more complex. Even though the presence of the anatase phase is detected by GIXRD only in the thickest film regions (figure14(b)), a detailed surface structure inspection by microscopy reveals that the film consists of round/cone shaped crystallites with a surface coverage in the amorphous matrix depending on the location in the deposited wafer (figures 15(c) and (d)).

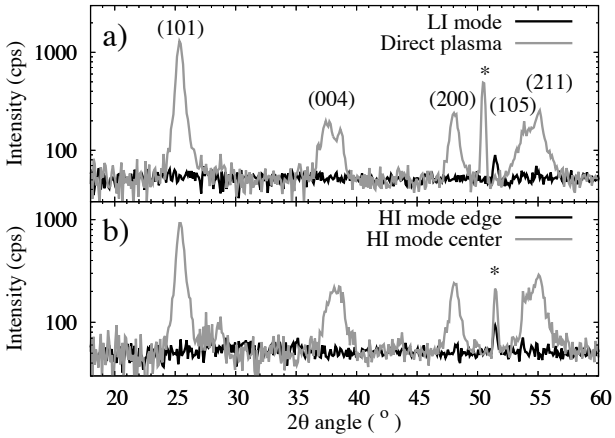

Figure 14. The GIXRD patterns of the PEALD TiO_2 films deposited with a) low-intensity mode (LI) and direct plasma, b) high-intensity mode plasma (HI), measured from the thickest film region (center) and at the edge of the deposited wafer. The reflections denoted with asterisk (∗) are of instrumental origin.

In thermal ALD a temperature of 150 °C has typically been considered as the lower limit for crystal agglomeration of TiO_2 with $TiCl_4$ and water [62]. With O_2 plasma PEALD (partially crystalline) films with anatase phase have been obtained at temperatures below 100 °C using ICP PEALD reactors [31, 63]. Besides the deposition temperature and the substrate material, it has been presented that the TiO_2 crystallization is strongly dependent on the flux of ions on the deposition surface,

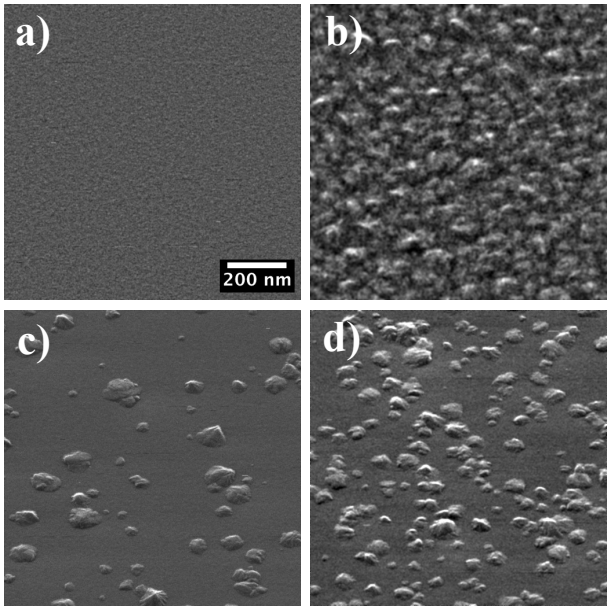

Figure 15. The surface structure HIM images of the TiO_2 films deposited with a) low-intensity mode, b) direct plasma, and c) and d) high-intensity mode plasma, samples from the edge (c) and in the middle (d) of the wafer. The samples are tilted to 45° and the scale bar is 200 nm.

and can be controlled either by adjusting the operating pressure [63] or by substrate-biasing [64, 65, 66], both affecting the energy of the ions bombarding the surface. This corresponds with the results obtained for the TiO_2 films deposited under different plasma conditions, where the amorphous film was achieved by preventing the ion bombardment to the substrate and the introduction of the direct plasma resulted in fully crystalline film.

4. Discussion

The observations of the different plasma modes and their effects with respect to the PEALD of ZnO and TiO_2 films imply that in the high-intensity mode a local region where the conditions are similar to the direct plasma is formed on the deposition surface. This so called "parasitic" discharge between the grid and the substrate can be associated to the existence of α and γ modes in the CCP. As described earlier, the α and γ modes are defined by the main ionization process sustaining the discharge, and whether the ionization is supported in the bulk of the plasma (α mode) or in the near-electrode sheaths (γ mode). In the used measurement setup the optical emission was measured perpendicular to the electrode surfaces and could therefore not distinct between emission originating from the sheath and bulk plasma regions. The characteristics of each mode can still be drawn from the OES as well as from the observations made from the PEALD films.

The observed low-intensity mode corresponds to the α mode. Based on the

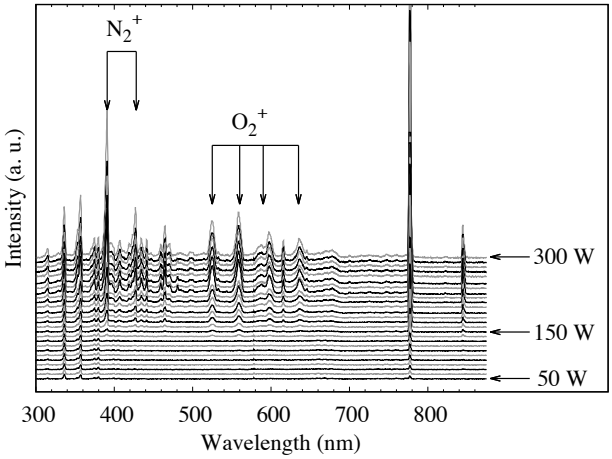

Figure 16. The optical emission spectra of the low-intensity mode at delivered powers of 50–300 W.

measured OES spectra and the corresponding rate coefficient analysis, the electron temperature T_e in this mode is moderate (< 3 eV), typical for capacitive discharges used in materials processing [3]. The studies of α mode have shown a uniform, fairly low-intensity discharge [16, 17, 19]. At low powers the plasma covers the electrode area partially (normal glow region), and the coverage widens when the power input is increased [16]. The plasma parameters such as the current and power density remain somewhat constant until the whole electrode area is covered (abnormal glow) and the current density starts to increase [16, 19]. Without measuring the current-voltage characteristics this behavior of the α mode can be inferred from the measured self-bias values in figure 3 and corresponding OES spectra measured as a function of the delivered power (figure 16). As seen in figure 3 the self-bias of the low-intensity mode plasma increases linearly until ca. 120 W without fluctuations and the corresponding spectra measured at each data point (figure 16) look similar. From the spectra measured with higher delivered powers it can be seen that besides of the increase in the dominant 777 nm peak intensity also peaks resulting from the excited O_2^+ and N_2^+ ions emerge, indicating increased plasma density and electron energy due to increased power density.

The uniform thicknesses of the PEALD films deposited in the low-intensity mode, both with remote and direct plasma configurations also illustrate the uniformity of the discharge. In the remote PEALD the ions passing through the grid holes lose their energy or recombine in the collisions in the gas volume between the grid and the deposition surface, and thus the film growth is governed mainly by the neutral plasma radicals. In the direct plasma conditions the energy of the bombarding ions, which is largely defined by the plasma potential, provide additional energy to the film growth, i. e. by enhancing the crystallinity [63] and growth rate.

The connection between the observed high-intensity mode and the γ mode can also be vindicated. The increase in total optical intensity implies a surge in the energy density of the plasma. Similar drastic increase in the overall emission intensity in the case of α–γ

mode transition has been reported e.g. by Moon et al. [16] who also presented intensity profiles of the plasma operated in both modes, and showed that the near-electrode sheath is the source of the bright emission. Based on the OES and rate coefficient analysis it is deduced that the line-integrated electron temperature increases when the transition to the high-intensity γ mode occurs, substantiating e.g. the electronic excitation rate of the N_2 molecules. This is presumably due to the change of the EEDF towards a bi-Maxwellian form, consisting of low-energy electrons created in the ionization and the tail of hot electrons gaining and depositing energy in the plasma sheath. The bi-Maxwellian EEDF of the γ mode in molecular gas capacitive disharges has also been measured directly by Abdel-Fattah et al. [67]. The energetic electrons can be considered as the source of the parasitic discharge between the grid and the deposition surface. In the γ mode at moderate pressures the plasma sheath undergoes a breakdown, and the electrons generated by the ion bombardment of the electrodes can have energies up to tens of eV [21]. These electrons, having energies greater than the sum of the plasma potential and the ionization potential are able to penetrate through the grid holes and ionize the gas beneath it, creating and sustaining an active plasma below the grid. It has been reported that the (grounded) grid prevents passing of electrons if the diameter of the holes is smaller than twice the plasma sheath thickness at the grid [68]. This condition is not met in the γ mode where the plasma sheath suffers a breakdown or its thickness is drastically reduced, depending on the operating pressure.

The locality of the measured differences in the PEALD films also supports the hypothesis of the presence of the γ mode discharge. Several studies show that the spatial distribution of the plasma changes during the α–γ mode transition [16, 17, 19, 69]. In the γ mode the plasma volume contracts and the bright sheath region covers the electrode only partially, the discharge cross-sectional area being somewhat independent on the applied power [17, 19]. This contraction is also accompanied by a significant surge in the power density (up to orders of magnitude), increase in the plasma resistivity, and reduction of the electron temperature in the plasma bulk [14, 17, 19, 70]. In addition the translational temperature of the neutral gas increases [17, 19], presumably affecting the PEALD growth. The natural feature of discharge contraction in the γ mode results in non-uniform plasma conditions over the deposition area being virtually independent on the PEALD processing parameters.

The contraction of the plasma and the subsequent change in the power density explain why both modes could be sustained at the same delivered power, the ignition to one of them being governed by the matching network settings. The increase of the plasma resistance in the γ mode was qualitatively determined from the operation parameters of the matching network capacitors C_L and C_T, where the $C_{L,\alpha} > C_{L,\gamma}$ while C_T was held constant (See Appendix). In the experiments it was also observed that the γ mode discharge generation appears to be sensitive to the pressure gradient, leading to the plasma contraction around the gas inlets in the powered showerhead electrode. The field of view to the plasma required for the OES measurements changed slightly the gas feed properties causing the generation of the γ mode discharge at the same location,

as seen in the deposited films, but the effect was visible also in the setup where the gas feed was divided uniformly through the showerhead area. This kind of "hot spot" effect, following the increase of the plasma power in the similar CCP PEALD setups has also been reported earlier [8]. However, the gas feed distribution had no effect in the α mode, and all the films deposited either with remote or direct plasma configuration had uniform thicknesses independent on the gas feed. In the direct plasma conditions the discharge did not develop into the γ mode within range of the applied power, regardless of the matching network tuning. This is most likely due to the surface properties of the silicon substrate that did not allow the secondary electron yield required for the γ mode discharge generation [13, 18].

5. Conclusions

The α and γ modes of the O_2–N_2 mixture capacitively coupled plasma used for the remote CCP PEALD were identified by means of optical emission spectroscopy and rate coefficient analysis. The results showed that the optical emission spectra of the α mode discharge are dominated by the atomic oxygen radicals (O^*) created predominantly as a result of the dissociative electron attachment process. In the γ mode the high-energy secondary electrons generated at the electrode surface increase the electron temperature in the plasma sheath, enhancing the electronic excitation of the N_2 molecules occupying the spectra. The effect of the α and γ modes on the PEALD was studied by deposition of ZnO and TiO_2 films. Of the observed modes only the α mode discharge provides desired conditions for PEALD due to the uniform discharge across the electrode area. If the discharge is allowed to undergo a transition to the γ mode, a parasitic discharge is generated between the grid and the substrate, leading to non-uniform film growth. However, in the remote plasma configuration where the grid separates the plasma volume from the deposition surface the concentration and/or the energy of the neutral plasma radicals may not be sufficient for the desired PEALD film growth and properties at low deposition temperatures. In the case of ZnO it was observed that the film composition was significantly different between the remote and direct plasma PEALD. The TiO_2 films instead had stoichiometric composition independent on the plasma conditions but the crystallinity was significantly enhanced in the direct plasma deposition due to the contribution of the ion bombardment during the film growth. The presence of the different plasma modes is important to acknowledge in the materials processing applications, as the transition to γ modes sets an upper limit to the delivered power/applied RF voltage in the cases where the uniform discharge is appreciated.

Acknowledgements

This work was supported by Academy of Finland Center of Excellence in Nuclear and Accelerator Based Physics (Ref. No. 251353), and is based on work from COST Action MP1402 'Hooking together European research in atomic layer deposition (HERALD)',

supported by COST (European Cooperation in Science and Technology). The authors acknowledge use of the Norwegian Centre for X-ray Diffraction, Scattering, and Imaging (RECX).

Appendix: Plasma resistance

Another feature of the mode transition of the studied discharge is the change of the plasma resistance between the two modes. The impedance matching of the RF power delivery system is implemented with the standard L-type matching circuit consisting of two adjustable capacitors, referred as 'load' and 'tune' capacitors C_L and C_T, respectively. For the standard circuit the capacitances are matching to a load $R + jX$, where R is the plasma resistance and jX is the imaginary component of the load impedance consisting of the circuit and stray capacitances and the inductance of the connecting cables. For the standard circuit the capacitances C_L and C_T can be expressed as

$$C_L = \frac{1}{2\omega R}\left[[1 - \left(1 - \frac{2R}{R_0}\right)^2\right]^{\frac{1}{2}} \text{, and} \tag{A.1}$$

$$C_T = \left(\omega X - \frac{1 - R/R_0}{C_L}\right)^{-1} , \tag{A.2}$$

where R_0 is 50 Ω and ω is the RF (angular) frequency [71]. For the purpose of defining the change in the plasma resistance between the α and γ modes it is sufficient to note that the C_L depends only on the plasma resistance R. From the (A.1) and (A.2) follows that if the C_T is held constant, the total plasma resistance R increases when the C_L decreases, which was observed in the plasma mode measurements, where $C_{L,\alpha} > C_{L,\gamma}$. This is consistent with the expected behaviour of the bulk plasma parameters T_e and n_e. The resistance $R = L/(\sigma A)$, where σ is the plasma conductivity, L is interelectrode separation, and A the discharge coverage area. The RF conductivity of plasma electrons σ_e can be expressed as

$$\sigma_\mathrm{e} = \frac{n_\mathrm{e} e^2}{m_\mathrm{e}\sqrt{\nu_\mathrm{e}^2 + \omega_\mathrm{RF}^2}} \cos\left(\omega t - \phi\right) , \tag{A.3}$$

where ν_e is the electron collision frequency. The DC part of the conductivity in the (A.3), omitting the RF frequency and the phase shift, can be considered as a good approximation of the plasma conductivity in the bulk plasma where the electric field is suppressed by the Debye shielding. The charged particle collisions affecting the conductivity of the weakly ionized O_2/N_2 plasmas are long-range effects due to the nature of the Coulomb interaction. The electron-electron and electron-ion collision frequencies $\nu_{\mathrm{e-e}}$ and $\nu_{\mathrm{e-i}}$, respectively, in (singly charged) low-temperature plasmas are proportional to the electron temperature and density as

$$\nu_{\mathrm{e-e,e-i}} \propto \frac{n_\mathrm{e}}{(kT_\mathrm{e})^{\frac{3}{2}}} . \tag{A.4}$$

Thus, it follows from (A.3) and (A.4) that for the plasma resistance R

$$R \propto (kT_e)^{-\frac{3}{2}} \ . \tag{A.5}$$

The reduction of the bulk electron temperature associated with the plasma mode transition from α to γ mode can be expected to cause the plasma resistance to increase despite of the higher local electron density. The effect to the resistance is further enhanced due to the contracted discharge area in the γ mode.

References

[1] Leskelä M and Ritala M 2002 *Thin Solid Films* **409** 138
[2] Profijt H, Potts S E, van den Sanden M C M and Kessels W M M 2011 *Vacuum Sci. Tech.* A **29** 050801
[3] Liebermann M A and Lichtenberg A J 2005 *Principles of Plasma Discharges and Materials Processing* 2nd ed. (John Wiley & Sons, New York)
[4] Matsuda A and Tanaka K 1986 *J. Appl. Phys* **60** 2351
[5] Show T, Yabe Y, Izumi T and Yamauchi H 20015 *Diam. Relat. Mater* **14** 1848
[6] Kääriäinen T O and Cameron D C 2009 *Plasma Processes and Polymers* **6** S237
[7] Profijt H and Kessels W M M 2013 *ECS Trans.* **50** 23
[8] Bosund M, Sajavaara T, Laitinen M, Huhtio T, Putkonen M, Airaksinen V-M and Lipsanen H 2011 *Appl. Surf. Sci* **257** 7827
[9] Godyak V A and Piejak 1990 *Phys. Rev. Lett.* **65** 996
[10] You S J, Ahn S K and Chang H Y 2006 *Appl. Phys. Lett.* **89** 171502
[11] Abdel-Fattah E and Sugai H 2003 *Appl. Phys. Lett.* **83** 1533
[12] You S J, Kim H C, Chung C W, Chang H Y and Lee J K 2003 *J. Appl. Phys.* **94** 7422
[13] Odrobina I and Kando M 1996 *Plasma Sources Sci. Technol.* **5** 517
[14] Lisovskiy V A and Yegorenkov V D 2004 *Vacuum* **74** 19
[15] Belenguer P and Boeuf J P 1990 *Phys. Rev.*A **41** 447
[16] Moon S Y, Rhee J K, Kim D B and Choe W 2006 *Physics of Plasmas* **13** 033502
[17] Vidaud P, Durrani S M A, Hall D R 1988 *J. Phys. D: Appl. Phys* **21** 57
[18] Derzsi A, Korolov I, Schüngel E, Donk Z and Schulze J 2015 *Plasma Sci. Technol.* **24** 034002
[19] Yang X, Moravej M, Nowling G R, Babayan S E, Panelon J, Chang J P and Hicks R F 2005 *Plasma Sources Sci. Technol* **14** 314
[20] Godyak V A and Khanneh A S 1986 *IEEE Trans. Plasma Sci.* **14** 112
[21] Lisovskiy V A, Booth J-P, Landry K, Douai C, Cassagne V and Yegorenkov V D 2006 *Physics of Plasmas* **13** 103505
[22] Lisovskiy V A, Kharchenko N D and Yegorenkov V D 2010 *Vacuum* **2010** 782
[23] Lisovskiy V, Booth J-P, Landry K, Douai D, Cassagne V and Yegorenkov V 2007 *J. Phys. D: Appl. Phys.* **40** 6631
[24] Lisovskiy V, Booth J-P, Jolly J, Martins S, Landry K, Douai D, Cassagne V and Yegorenkov V 2007 *J. Phys. D: Appl. Phys.* **40** 6989
[25] Lisovskiy V, Yegorenkov V, Booth J-P, Martins S, Landry K, Douai D and Cassagne V 2012 *Physics Letters* A **376** 2238
[26] Kim D, Kang H, Kim J-M, Kim H 2011 *Appl. Surf. Sci.* **257** 3776
[27] Tynell T and Karppinen M *Semicond, Sci. Technol.* **29** 043001
[28] Thomas M A and Cui J B 2012 *ACS Appl. Mater. Interfaces* **4** 3122
[29] Tallarida M, Friedrich D, Städter M, Michling M and Schmeisser D 2011 *Nanoscience and Nanotechnology* **11** 8049
[30] Das C, Henkel K, Tallarida M, Schmeisser D, Gargouri H, Kärkkäinen I, Schneidewind J, Gruska B and Arens M 2015 *J. Vac. Sci. Technol.* A **33** 01A144

[31] Strobel A, Schnabel H-D, Reinhold U, Rauer S and Neidhart A 2015 *J. Vac. Sci. Technol.*A **34** 01A118-1

[32] Kubala N G and Wolden C A 2010 *Thin Solid Films* **518** 6733

[33] Laitinen M, Rossi M, Julin J and Sajavaara T 2014 *Nucl. Inst. Meth.* B **337** 55

[34] Arstila K et al. 2014 *Nucl. Inst. Meth.* B **331** 34

[35] Laporta V, Celiberto R and Tennyson J 2014 *AIP conf. Proc.* **1628** 939

[36] "Database for European Union Phys4Entry Project" 2012–2014 `http://users.ba.cnr.it/imip/cscpal38/phys4entry/database/html`

[37] Gudmundsson J T and Thorsteinsson E G 2007 *Plasma Sources Sci. Technol.* **16** 399

[38] Laporta V, Celiberto R and Tennyson J 2013 *Plasma Sources Sci. Technol.* **22** 025001

[39] Itikawa Y and Ichimura A 1990 *Phys. Chem. Ref. Data* **19** 637

[40] Laher L and Gilmore F 1990 *Phys. Chem. Ref. Data* **19** 277

[41] Ishikawa T, Hayashi D, Sasaki K and Kadota K 1998 *Appl. Phys. Lett.* **72** 2392

[42] Zhou X and Dickinson A S 1997 *Nucl. Inst. Meth.* B **124** 5

[43] You Z, Dai Z and Wang Y 2014 *Plasma Sci. Technol.* **16** 335

[44] Itikawa Y and Ichimura A 2009 *J. Phys. Chem. Ref. Data* **38** 1

[45] Itikawa Y 2006 *J. Phys. Chem. Ref. Data* **35** 31

[46] Lofthus A and Krupenie P H 1977 *J. Phys. Chem. Ref. Data* **6** 113

[47] Krames B, Glenewinkel-Meyer T and Meischner J 2001 *J. Phys. D: Appl. Phys.* **34** 1789

[48] Zhang J, Yang H, Zhang Q-L, Dong S and Luo J K 2013 *Appl. Surf. Sci* **282** 390

[49] Jin M-J, Jo J, Neupane G P, Kim J, An K-S, Yoo J-W 2013 *AIP Advances* **3** 102114

[50] Rowlette P C, Allen C G, Bromley O B, Dubetz A E and Wolden C A 2009 *Chem. Vap. Deposition* **15** 15

[51] Zhang X, Qin J, Hao R, Wang L, Shen X, Yu R, Limpanart S, Ma M and Liu R 2015 *J. Phys. Chem.* C **119** 20544

[52] Wöll C 2007 *Progress in Surface Science* **82** 55

[53] Coutts T J, Li X, Barnes T M, Keyes B M, Perkins C L, Asher S E, Zhang S B, Wei S-U and Limpijumnong S 2006 *Chapter 3 in 'Zinc Oxide Bulk, Thin Films and Nanosctructures'* ed Jagadish C and Pearton S (Oxford, Elsevier Science Ltd.)

[54] Zou C W, Yan X D, Han J, Chen R Q, GaO W and Metson J 2009 Appl. Phys. Lett **94** 171903

[55] Kawamura Y, Hattori N, Miyatake N and Uraoka Y 2013 *J. Vacuum Sci. Tech.* A **31** 01A142

[56] Langereis E, Kejmel J, van den Sanden M C M and Kessels W M M 2008 *Appl. Phys. Lett.* **92** 231904

[57] Potts S E, Profijt H B, Roelofs R and Kessels W M M 2013 *Chem. Vap. Deposition.* **19** 1

[58] Malm J, Sahramo E, Perälä J, Sajavaara T and Karppinen M 2011 *Thin Solid Films* **519** 5319

[59] Bergum K, Fjellvåg and Nilsen O 2015 *Appl. Surf. Sci* **332** 494

[60] Pung S-W, Choy K-W, Hou X, Shan C 2008 *Nanotechnology* **19** 435609

[61] Singh T, Lehnen T, Leuning T, Sahu D, Mathur S 2014 *Appl. Surf. Sci* **289** 27

[62] Miikkulainen V, Leskelä M, Ritala M and Puurunen R L 2013 *J. Appl. Phys* **113** 021301

[63] Ratzsch S, Kley E-B, Tünnermann and Szeghalmi 2015 *Nanotechnology* **26** 024003

[64] Profijt H B, van den Sanden M C M and Kessels W M M 2012 J. Vac. Sci. Technol.A **31** 01A106

[65] Ratzsch S, Kley E-B, Tünnermann and Szeghalmi A 2015 *Materials* **8** 7805

[66] Profijt H B, van de Sanden and Kessels 2012 *Electrochem. Solid-State Lett.* **15** G1

[67] Abdel-Fattah E and Farang O F 2013 *Can. J. Phys* **91** 1062

[68] Hong J I, Seo S H, Kim S S, Yoon N S, Chang C S and Chang H Y 1999 *Physics of Plasmas* **6** 1017

[69] Moon S Y, Rhee J K, Kim D B, Gweon B M and Choe W 2009 Current Applied Physics **9** 274

[70] Xu Y, Yu W, Jiang Z, Li Y, Li H and Feng H 2014 *Thin Solid Films* **569** 52

[71] Chen F C 1992 *Capacitor Tuning Circuits for Inductive Loads* `http://www.seas.ucla.edu/~ffchen/Publs/Chen144.pdf`